FAST TRACK COMMUNICATIONS

Surface chemical bonding states and ferroelectricity of Ce-doped BiFeO$_3$ thin films prepared by sol–gel process

**Zuci Quan · Hao Hu · Sheng Xu · Wei Liu ·
Guojia Fang · Meiya Li · Xingzhong Zhao**

Abstract Bi$_{1-x}$Ce$_x$FeO$_3$ (x = 0, 0.05, 0.1, 0.15 and 0.20) (BCFO) thin films were deposited on Pt/TiN/Si$_3$N$_4$/Si substrates by sol–gel technique. Crystal structures, surface chemical compositions and bonding states of BCFO films were investigated by X-ray diffraction and X-ray photoelectron spectroscopy (XPS), respectively. Compared to BiFeO$_3$ (BFO) counterparts, the fitted XPS narrow-scan spectra of Bi 4f$_{7/2}$, Bi 4f$_{5/2}$, Fe 2p$_{3/2}$, Fe 2p$_{1/2}$ and O 1s peaks for Bi$_{0.8}$Ce$_{0.2}$FeO$_3$ film shift towards higher binding energy regions by amounts of 0.33, 0.29, 0.43, 0.58 and 0.49 eV, respectively. Dielectric constants and loss tangents of the BCFO (x = 0, 0.1 and 0.2) film capacitors are 159, 131, 116, 0.048, 0.041 and 0.035 at 1 MHz, respectively. Bi$_{0.8}$Ce$_{0.2}$FeO$_3$ film has a higher remnant polarization (P_r = 2.04 μC/cm^2) than that of the BFO (P_r = 1.08 μC/cm^2) at 388 kV/cm. Leakage current density of the Bi$_{0.8}$Ce$_{0.2}$FeO$_3$ capacitor is 1.47×10^{-4} A/cm^2 at 388 kV/cm, which is about two orders of magnitude lower than that of the BFO counterpart. Furthermore, Ce cations are feasibly substituted for Bi^{3+} in the Bi$_{0.8}$Ce$_{0.2}$FeO$_3$ matrix, possibly resulting in the enhanced ferroelectric properties for the decreased grain sizes and the reduced oxygen vacancies.

Keywords BiFeO$_3$ thin films · Ce-doping ·
Surface chemical bonding states ·
Dielectric and ferroelectric properties

Z. Quan · H. Hu · S. Xu · W. Liu · G. Fang · M. Li ·
X. Zhao (✉)
Key Laboratory of Acoustic and Photonic Materials and Devices
of Ministry of Education, Department of Physics, Wuhan
University, Wuhan 430072, People's Republic of China
e-mail: xzzhao@whu.edu.cn

1 Introduction

ABO$_3$-type perovskite structure BiFeO$_3$ (BFO) has attracted much attention because it is a known Pb-free and environmentally friendly material that simultaneously shows electric and magnetic ordering in the same phase [1–3]. Based on the specific characteristics, including magnetoelectric coupling effects [1], high Curie temperature ($T_C \sim$ 1,103 K) and Néel temperature ($T_N \sim$ 643 K) [4], and small optical bandgap ($E_g \sim$ 2.5 eV) [5], BFO thin films have potential applications in magnetic/ferroelectric data storage media, spintronics, nonvolatile memories, photocatalytic compound and ultrafast optoelectronic devices [1, 3, 5, 6]. Though as promising as BiFeO$_3$ films are, there are still drawbacks, such as large dielectric loss, small remnant polarization, high coercive field, high leakage current and inhomogeneous magnetic spin structure [4, 7, 8], to be overcome before practical applications. One way of doing so is by doping BFO films with other elements. In order to enhance ferroelectric properties, reduce leakage current, modify its spatially inhomogeneous spin-modulated incommensurate structure, and intensify magnetoelectric interaction, several research groups have tried A-site, B-site or (A, B)-sites of BFO films substituting by La [2, 7], Tb [9], Gd [10], Sc [4], Ti [11], Cr [12], La and Ti [13], La and Mn [14] as well as La and Nb [15]. More recently, Shannigrahi et al. reported that impure phase appeared in 0.5 mol% Sc-doped BFO film, and leakage current, ferroelectric and magnetic properties were improved for 0.3 mol% Sc-doped BFO [4]. Wang et al. investigated that Ti^{4+} ions were used to substitute some of Fe cations to form Ti$_{Fe}^{\bullet\bullet}$ as substituting Fe^{2+} or Ti$_{Fe}^{\bullet}$ as substituting Fe^{3+}, which could eliminate oxygen vacancies in the Ti-doped BFO films because of the requirements of charge compensation [11]. Cheng et al. found that the

ferroelectric properties were significantly improved, and the ferromagnetic moments were kept at a high level for the (La, Nb)-codoped BFO films [15]. Being a lanthanide element, however, Ce has remained relatively unexplored in doping BFO films.

In this study, crystal structures, surface chemical compositions and bonding states of pure and Ce-doped BFO films were characterized by X-ray diffraction (XRD) and X-ray photoelectron spectroscopy (XPS), respectively. Chemical shifts of Bi $4f_{7/2}$, Bi $4f_{5/2}$, Fe $2p_{3/2}$, Fe $2p_{1/2}$, O 1s, Ce $3d_{5/2}$ and Ce $3d_{3/2}$ peaks for pure BFO and $Bi_{0.8}Ce_{0.2}FeO_3$ films were analyzed by fitting the corresponding XPS narrow-scan spectra. Dielectric and ferroelectric properties of the pure and Ce-doped BFO film capacitors were also discussed.

2 Experimental details

Bismuth nitrate [$Bi(NO_3)_3 \cdot 5H_2O$], iron nitrate [$Fe(NO_3)_3 \cdot 9H_2O$] and cerium nitrate [$Ce(NO_3)_3 \cdot 6H_2O$] were suitably dissolved in the mixtures of 2-methoxyethanol ($CH_3OCH_2CH_2OH$) and glacial acetic acid (CH_3COOH), while Ce contents were determined by composition formulae $Bi_{1-x}Ce_xFeO_3$ (abbreviated as BCFO), where x is equal to 0 (for pure BFO), 0.05, 0.10, 0.15 and 0.20, respectively. Meanwhile, acetylacetone ($CH_3COCH_2COCH_3$) and N-N-dimethyl formamide [$(CH_3)_2NOCH$] in 1 to 1 molar ratio with respect to $Fe(NO_3)_3 \cdot 9H_2O$ were used to stabilize BCFO solutions. The stock solutions were stirred at 318 K for 240 min to obtain homogeneous BCFO precursors. BCFO sols were spin-coated onto Pt (111)/TiN/Si_3N_4/Si (100) substrates at 3,000 rpm for 20 s. After each spin-coating, the green BCFO films were dried at 393 K for 10 min, and then prebaked at 693 K for 30 min in the air to remove organic contaminations. This procedure was repeated several times to obtain appropriate thickness. Finally, BCFO films were annealed in a quartz tube furnace at 873 K for 60 min under a N_2 ambience, and then cooled down slowly to room temperature.

Crystal structures of BCFO films were analyzed by XRD (D8 Advance, Bruker Corp.) with Cu K_α radiation. Thicknesses of BCFO films were measured by scanning electron microscope (SEM) (Sirion FEG, FEI Co.). Surface chemical compositions and bonding states of the corresponding elements for BFO and $Bi_{0.8}Ce_{0.2}FeO_3$ films were investigated by XPS (VG MultiLab 2000, Thermo Electron Corp.). The XPS Al K_α source operating at 300 W provided nonmonochromatic X-rays at 1,486.6 eV. Photoelectric peak of C 1s located at 284.6 eV was assigned to carbon from adventitious contaminations, and it was used as the criterion to rectify binding energies of XPS spectra. Software of XPSPEAK Version 4.1 was used to fit the narrow-scan

spectra of Bi 4f, Fe 2p, O 1s and Ce 3d after Shirley-type background subtraction [16, 17]. For comparison, 120-nm-thick Pt top electrodes with diameter of 0.3 mm were sputtered on BCFO films through a metal shadow mask. To understand Ce-doped influence on dielectric and ferroelectric properties of BFO film, capacitance-frequency and dielectric loss-frequency curves for the BCFO ($x = 0$, 0.1 and 0.2) film capacitors were measured by a precision impedance analyzer (Agilent 4294A, Agilent Technologies Ltd.). Polarization–electric field (P–E) hysteresis loops and leakage current density–electric field (J–E) curves for the same BCFO capacitors were measured by a precision materials analyzer (RT6000, Radiant Technology Inc.). All measurements were carried out at room temperature.

3 Results and discussion

Figure 1 shows XRD patterns of BCFO films annealed in 873 K for 60 min under a N_2 ambience. It is found that all the BCFO films are polycrystalline and exhibit a single-phase perovskite structure. Non-perovskite phase such as $Bi_2Fe_4O_9$, $Bi_{36}Fe_2O_{57}$ and $Bi_{12}(Bi_{0.5}Fe_{0.5})O_{19.5}$ [6, 18] are not detected in the XRD patterns. The obvious peak-splitting XRD pattern for the BCFO film with $x = 0$ indicate that the BFO film is rhombohedral phase (space group $R3c$) [10]. As shown in the broken square of Fig. 1, (104) and (110) peaks of BCFO films move closer together along with broadening, indicating a structural change [19, 20] with increasing Ce content. Since ionic radii of Ce^{3+} (1.18 Å) and Ce^{4+} (1.02 Å) are smaller than that of Bi^{3+} (1.20 Å) [21], Ce cations are partially substituted for Bi^{3+}
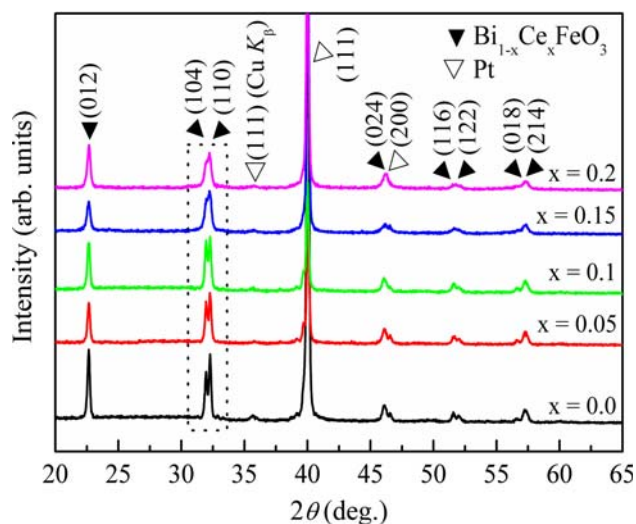

Fig. 1 XRD patterns of $Bi_{1-x}Ce_xFeO_3$ ($x = 0$, 0.05, 0.1, 0.15 and 0.2) films deposited on Pt/TiN/Si_3N_4/Si substrates. As shown in the broken square of Fig. 1, (104) and (110) peaks merge when x increases from 0 to 0.2

with increasing Ce dopant, resulting in smaller grain sizes of the BCFO films compared to those of the BFO counterparts.

Figure 2 shows XPS survey spectra of BFO and $Bi_{0.8}Ce_{0.2}TiO_3$ films. There are XPS photoelectron peaks and the corresponding Auger lines of Bi, Fe, O and C elements on the BFO film surface. Herein, C 1s peak located at 284.6 eV is used as the criterion to rectify the binding energy of XPS spectra. Characteristic peaks for Bi $4f_{7/2}$ (158.56 eV), Bi $4f_{5/2}$ (163.90 eV), Fe $2p_{3/2}$ (710.33 eV), Fe $2p_{1/2}$ (723.69 eV), O 1s (529.52 eV) and Auger peaks for Fe $L_3M_{45}M_{45}$ (783.86 eV), Fe $L_3M_{23}M_{45}$ (838.24 eV) and Fe $LM_{23}M_{23}$ (888.29 eV) [17] are identified in Fig. 2. Undoubtedly, there is no signal of Ce element in the pure BFO film. As for $Bi_{0.8}Ce_{0.2}FeO_3$ film, there are XPS signals of Bi, Ce, Fe, O and C elements, where Ce $4d_{5/2}$ (108.71 eV), Ce $4d_{3/2}$ (112.43 eV), Ce $3d_{5/2}$ (882.32 eV) and Ce $3d_{3/2}$ (900.64 eV) and Auger peak for Ce $M_{45}N_{45}N_{45}$ (832.87 eV) [17] are assigned in Fig. 2. It is concluded that some Ce–O bonds are present in $Bi_{0.8}Ce_{0.2}FeO_3$ matrix.

Figure 3 shows the fitted narrow-scan spectra of Bi 4f, Fe 2p, O 1s and Ce 3d peaks for the BFO and $Bi_{0.8}Ce_{0.2}FeO_3$ films. Figure 3a(1) shows that pure Bi 4f doublet consists of two peaks at 158.56 and 163.90 eV, which are mainly identified as a signal from Bi–O bonds [17]. Spin-orbit splitting energy (Δ) of the pure Bi 4f doublet is 5.34 eV, which is comparable to theoretical value ($\Delta_{Bi\ 4f}$) of 5.31 eV [16]. Two fitted subpeaks located at 158.28 and 163.61 eV are ascribed to Bi $(4f_{7/2})$–O and Bi $(4f_{5/2})$–O bonds, while other subpeaks located at 158.84 and 164.18 eV may be related to Bi–O–Fe bonds in oxygen octahedron and/or relaxed Bi phase, probably caused by

Fig. 2 XPS survey spectra of BFO and $Bi_{0.8}Ce_{0.2}FeO_3$ films annealed at 873 K for 60 min under a N_2 ambience

oxygen vacancies and cation defects [17, 22]. Figure 3a(2) shows that compared to the pure Bi 4f doublet, Bi $4f_{7/2}$ (158.89 eV) and Bi $4f_{5/2}$ (164.19 eV) peaks of the $Bi_{0.8}Ce_{0.2}FeO_3$ film shift towards higher binding energy regions by amounts of 0.33 and 0.29 eV, respectively. Herein, two subpeaks located at 158.56 and 163.86 eV are ascribed to Bi $(4f_{7/2})$–O and Bi $(4f_{5/2})$–O bonds, while other subpeaks located at 159.22 and 164.52 eV may be related to Bi–O–Fe and Bi–O–Ce bonds in oxygen octahedron and/ or relaxed Bi phase. It is conceivable that Ce cations are substituted for Bi^{3+} at A-site in the $Bi_{0.8}Ce_{0.2}FeO_3$ matrix because of the decreased Bi 4f peak area in comparison with the pure counterpart. As reported by Gao et al., the N-doped Ba $3d_{5/2}$ and Ba $3d_{3/2}$ peaks shift towards the lower binding energy regions because the bonding energies of Ba–N bonds are lower than that of Ba–O bonds considering the slightly lower electronegativity of N element (3.04) than that of O element (3.44) [21]. So the chemical shifts of Bi 4f, Fe 2p and O 1 s peaks for the $Bi_{0.8}Ce_{0.2}FeO_3$ film may be related to the various electronegativity values for Bi (2.02), Ce (1.12), Fe (1.83) and O (3.44) elements [16, 21, 23]. To estimate ionicity of Bi–O, Ce–O and Fe–O bonds for the $Bi_{0.8}Ce_{0.2}FeO_3$ film, fraction of ionicity (F_i) [24] is given by:

$$F_i = 1 - \exp\left[-\frac{(\Delta EN)^2}{4}\right] \tag{1}$$

where ΔEN is difference in the anion and cation electronegativities. According to Eq. (1), the fraction of ionicity $[F_i(Ce–O)]$ (0.74) is much larger than $F_i(Bi–O)$ (0.40), and bonding energy of (Bi,Ce)–O bond in oxygen octahedron may be larger than that of single Bi–O bond, suggesting that the Bi 4f doublet of $Bi_{0.8}Ce_{0.2}FeO_3$ film shifts to the higher binding energy region.

Figure 3b shows the fitted Fe 2p narrow-scan spectra for the BFO and $Bi_{0.8}Ce_{0.2}FeO_3$ films. In Fig. 3b(1), the pure Fe 2p doublet consists of two wide peaks of Fe $2p_{3/2}$ (710.33 eV) and Fe $2p_{1/2}$ (723.69 eV), which are mainly ascribed to Fe–O bonds [17]. Spin-orbit splitting energy of the pure Fe 2p doublet is equal to 13.36 eV, which is compared to theoretical value ($\Delta_{Fe\ 2p}$) of 13.6 eV for Fe_2O_3 [17]. Figure 3b(2) shows that compared to the pure Fe 2p doublet, Fe $2p_{3/2}$ (710.76 eV) and Fe $2p_{1/2}$ (724.27 eV) peaks of the $Bi_{0.8}Ce_{0.2}FeO_3$ film shift towards higher binding energy regions by amounts of 0.43 and 0.58 eV, respectively. Herein, two subpeaks located at 711.51 and 725.15 eV are ascribed to (Fe $2p_{3/2})_2$–O_3 and (Fe $2p_{1/2})_2$–O_3 bonds, while the subpeaks located at 710.00 and 723.38 eV may be related to Fe–O bonds for Fe^{2+}, Fe–O–Bi bonds, Fe–O–Ce bonds in oxygen octahedra and/or other relaxed Fe phase [16, 25]. It is the reason why the Fe $2p_{3/2}$ and Fe $2p_{1/2}$ peaks of the $Bi_{0.8}Ce_{0.2}FeO_3$ film shift towards the higher binding energy

Fig. 3 The fitted XPS narrow-scan spectra of (**a**) Bi 4f, (**b**) Fe 2p, (**c**) O 1 s and (**d**) Ce 3d peaks for (1) BFO and (2) $Bi_{0.8}Ce_{0.2}FeO_3$ films. The black solid lines represent experimental result, red short dots represent the fitting results after Shirley-type background subtraction, the dashed peaks with colors of blue, magenta, violet and green are fitted subpeaks. Iterations are performed until a minimum for square of the difference (χ^2) between the experimental curve and the fitted curve is reached for each fitted sum curve
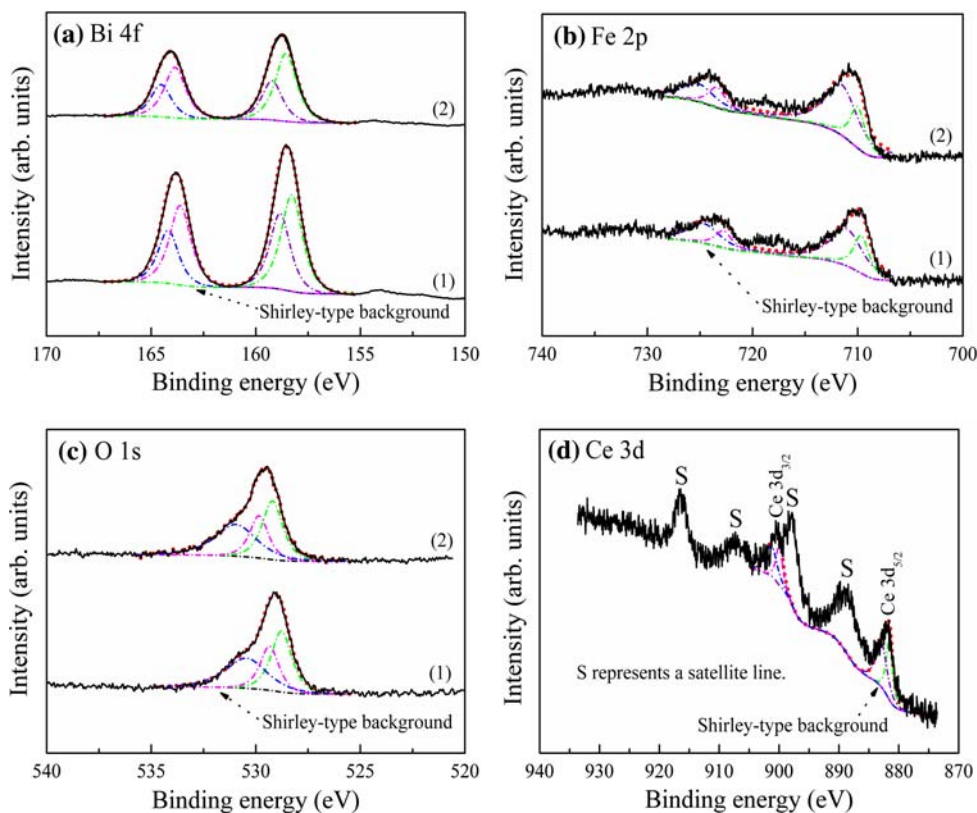
regions in comparison with the Fe 2p doublet of the BFO film. According to ratio of the fitted peak areas for Fe^{3+} and Fe^{2+}, concentration ratios of Fe^{3+} and Fe^{2+} in the BFO and $Bi_{0.8}Ce_{0.2}FeO_3$ films are 67:33 and 70:30, respectively, indicating that the presence of Fe^{2+} ions are less in the $Bi_{0.8}Ce_{0.2}FeO_3$ film compared to that of the BFO film. This could be an evidence for the decreased oxygen vacancies in the $Bi_{0.8}Ce_{0.2}FeO_3$ film.

Figure 3c shows the fitted O 1s narrow-scan spectra for the BFO and $Bi_{0.8}Ce_{0.2}FeO_3$ films. Figure 3c(1) shows that a broad O 1s peak (529.52 eV) for the BFO film consists of three subpeaks located at 528.77, 529.34 and 530.45 eV. Since the BFO film consists of three components (Bi_2O_3, Fe_2O_3 and FeO) in BFO solid solution, the subpeaks are mainly ascribed to $Fe_2–(O 1s)_3$ (529.6 eV), $Fe–(O 1s)$ (529.8 eV), $Bi_2–(O 1s)_3$ (530.0 eV) bonds [17] and relaxed O phase, especially for the fitted subpeak located at the higher binding energy region. It may be mainly attributed to the absorbed oxygen (531.0 eV) [17] associated with oxygen vacancies and surface species, such as H_2O and CO_2 absorbed from the air during the sol–gel process [16, 17]. Figure 3c(2) shows that compared to the counterpart of the BFO film, O 1s peak (530.01 eV) for the $Bi_{0.8}Ce_{0.2}FeO_3$ film shifts towards higher binding energy region by amount of 0.49 eV. These subpeaks are mainly ascribed to $Fe_2–(O 1s)_3$ (529.6 eV for the O 1s peak), $Fe–(O 1s)$ (529.8 eV), $Bi_2–(O 1s)_3$ (530.0 eV) and $Ce_2–(O 1s)_3$

(530.3 eV) bonds [17]. Considering that Ce^{3+} ions are partially substituted for Bi^{3+} ions, and binding energy of O 1s in $Ce_2–(O 1s)_3$ bond is larger than that of $Bi_2–(O 1s)_3$ bond, suggesting that the O 1s peak of the $Bi_{0.8}Ce_{0.2}FeO_3$ film shifts toward the higher binding energy regions in comparison with the BFO counterpart.

Figure 3d shows the fitted Ce $3d_{5/2}$ peak located at 882.24 eV and Ce $3d_{3/2}$ peak located at 900.61 eV. Both of them are mainly assigned to Ce–O bonds. Spin-orbit splitting energy of the Ce 3d doublet is equal to 18.37 eV, which is compared to theoretical value ($\Delta_{Ce\ 3d}$) of 18.10 eV for Ce or 18.30 eV for CeO_2 [17]. The fitted area ratio for Ce $3d_{5/2}$ and Ce $3d_{3/2}$ peaks is about 1.47, which is comparative to theoretical value of 1.50 for Ce 3d doublet [17]. Figure 3d also shows that each of the Ce 3d peak is accompanied by two satellite lines, called $3d^94f^0$ and $3d^94f^2$ [17, 26]. Furthermore, each of the Ce $3d_{5/2}$ and Ce $3d_{3/2}$ peak could be fitted by two subpeaks separated by 1.33 ± 0.01 eV. The subpeaks located at 882.91 and 901.27 eV are assigned to Ce $3d_{5/2}$–O and Ce $3d_{3/2}$–O bonds for Ce^{3+}. Meanwhile, the subpeaks located at 881.57 and 899.95 eV may be associated with Ce $3d_{5/2}$–O and Ce $3d_{3/2}$–O bonds for Ce^{4+} [17], (Bi, Ce)–O bonds and/or relaxed Ce phase, probably caused by oxygen vacancies and other defects.

Figure 4 shows typical dielectric properties of the BCFO (x = 0, 0.1 and 0.2) film capacitors at the measured frequency ranging from 40 Hz to 1 MHz. The
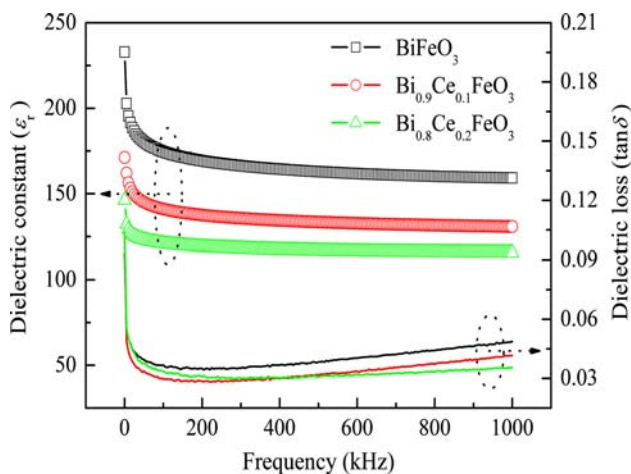
Fig. 4 Dielectric constants and loss tangents of $Bi_{1-x}Ce_xFeO_3$ ($x = 0$, 0.1 and 0.2) film capacitors as a function of frequency ranging from 40 Hz to 1 MHz

corresponding dielectric constant (ε_r) and loss tangent ($\tan\delta$) for the BFO, $Bi_{0.9}Ce_{0.1}FeO_3$ and $Bi_{0.8}Ce_{0.2}FeO_3$ capacitors are 159, 131, 116, 0.048, 0.041 and 0.035 at 1 MHz, respectively. It means that compared to the BFO counterparts, both ε_r and $\tan\delta$ of the $Bi_{0.8}Ce_{0.2}FeO_3$ capacitor decrease when 20 mol% Ce doped into the BFO matrix. Moreover, this result could be comparable to the values of PLD-derived $Bi_{0.8}La_{0.2}FeO_3$ ($\varepsilon_r = 86$, $\tan\delta = 0.69$) and $Bi_{0.8}La_{0.2}Nb_{0.01}Fe_{0.99}O_3$ ($\varepsilon_r = 184$, $\tan\delta = 0.038$) films [15] deposited on Pt/Ti/SiO$_2$/Si substrates at 100 kHz as reported by Cheng et al., respectively.

Figure 5 shows P–E hysteresis loops for the BFO, $Bi_{0.9}Ce_{0.1}FeO_3$ and $Bi_{0.8}Ce_{0.2}FeO_3$ film capacitors. These capacitors have typical ferroelectric characteristics, and the corresponding remnant polarization [$P_r = (P_r^+ - P_r^-)/2$]
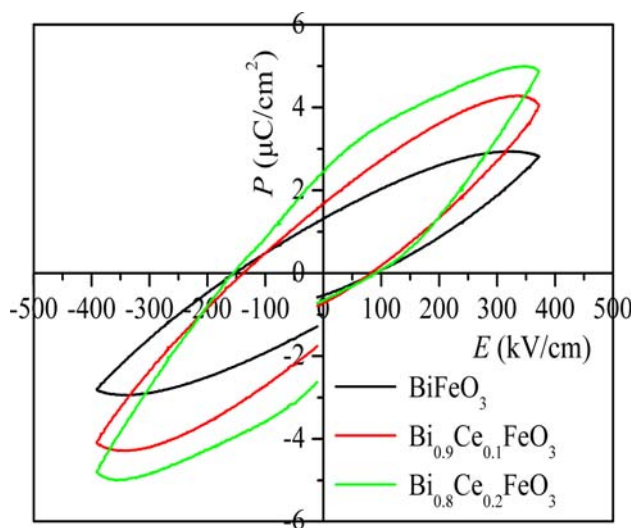
of 1.08, 1.43 and 2.04 μC/cm^2 and coercive field [$E_c = (E_c^+ - E_c^-)/2$] of 120, 112 and 123 kV/cm, respectively, are obtained under the applied electric field of 388 kV/cm. P_r value of the $Bi_{0.8}Ce_{0.2}FeO_3$ capacitor is larger than that of the BFO film, or those of the $BiFe_{1-x}Sc_xO_3$ ($x = 0.1$ and 0.3 mol%) films [4] or the Ti^{4+} and Ni^{2+} doped BFO films prepared by PLD process [27], but it is much small than that of the Gd-doped BFO film prepared by metal organic decomposition process [10]. According to Wang et al., ferroelectricity of BFO film originated from the displacements of Bi with respect to the FeO_6 cages along (111) plane [22]. Compared to the BFO counterpart, the increased P_r of the $Bi_{0.8}Ce_{0.2}FeO_3$ film might be attributed to the structural change in the oxygen octahedron, since Ce cations are feasibly substituted for Bi^{3+} as evidenced by the XPS spectra.

Figure 6 shows J–E curves of the BCFO ($x = 0$, 0.1 and 0.2) capacitors. Leakage current densities of BFO, $Bi_{0.9}Ce_{0.1}FeO_3$ and $Bi_{0.8}Ce_{0.2}FeO_3$ capacitors are 1.38×10^{-2}, 1.06×10^{-3} and 1.47×10^{-4} A/cm^2 at 388 kV/cm, respectively. It means that the leakage current density of the $Bi_{0.8}Ce_{0.2}FeO_3$ capacitor is about two orders of magnitude lower than that of the BFO counterpart. One reason for this is that an appropriate amount of Ce doping reduces grain sizes of the BCFO film as evidenced by XRD result, leading to an increase in the density of grain boundaries, which makes contribution to the decreased leakage current density [9]. Another reason is that the decreased Bi volatilization and the restrained reduction of Fe^{3+} to Fe^{2+} are realized by virtue of the reducible oxygen vacancies and cation defects after Ce-doping, as proofed by XPS data.
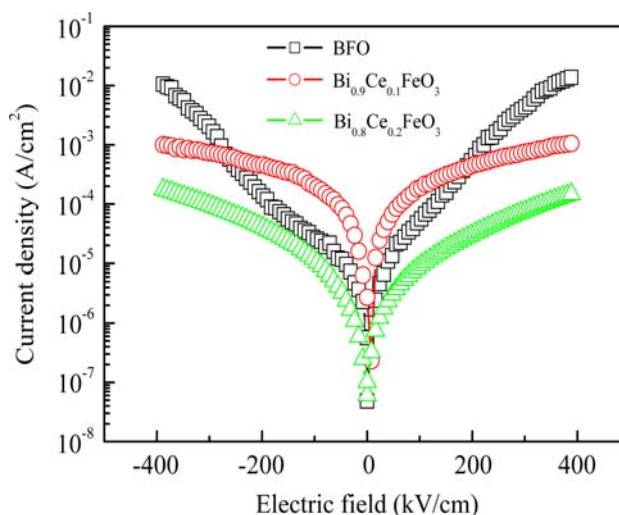

Fig. 5 Polarization-electric field hysteresis loops of $Bi_{1-x}Ce_xFeO_3$ ($x = 0$, 0.1 and 0.2) capacitors

Fig. 6 Leakage current density-electric field curves of $Bi_{1-x}Ce_xFeO_3$ ($x = 0$, 0.1 and 0.2) capacitors when electric filed ranges from -388 to 388 kV/cm

4 Conclusions

BCFO films were deposited on $Pt/TiN/Si_3N_4/Si$ substrates by sol–gel technique. Compared to the BFO counterparts, the fitted Bi $4f_{7/2}$, Bi $4f_{5/2}$, Fe $2p_{3/2}$, Fe $2p_{1/2}$ and O 1s peaks for the $Bi_{0.8}Ce_{0.2}FeO_3$ film shift towards the higher binding energy regions by amounts of 0.33, 0.29, 0.43, 0.58 and 0.49 eV, respectively. The corresponding ε_r and $\tan\delta$ of the BFO, $Bi_{0.9}Ce_{0.1}FeO_3$ and $Bi_{0.8}Ce_{0.2}FeO_3$ capacitors are 159, 131, 116, 0.048, 0.041 and 0.035 at 1 MHz, respectively. The corresponding P_r of 1.08, 1.43 and 2.04 $\mu C/cm^2$ and E_c of 120, 112 and 123 kV/cm are obtained under the electric field of 388 kV/cm, respectively. The leakage current density of the $Bi_{0.8}Ce_{0.2}FeO_3$ capacitor is about two orders of magnitude lower than that of the BFO counterpart. Compared to the BFO counterparts, the increased P_r and the decreased leakage current density of the $Bi_{0.8}Ce_{0.2}FeO_3$ film might be attributed to the decreased Bi volatilization and the restrained reduction of Fe^{3+} to Fe^{2+} by virtue of the reducible oxygen vacancies and cation defects after Ce-doping, as proved by the XPS spectra.

References

1. Zhao T, Scholl A, Zavaliche F, Lee K, Barry M, Doran A, Cruz MP, Chu YH, Ederer C, Spaldin NA, Das RR, Kim DM, Baek SH, Eom CB, Ramesh R (2006) Nat Mater 5:823
2. Chu YH, Zhan Q, Yang CH, Cruz MP, Martin LW, Zhao T, Yu P, Ramesh R, Joseph PT, Lin IN, Tian W, Schlom DG (2008) Appl Phys Lett 92:102909
3. Kumar A, Murari NM, Katiyar RS (2008) Appl Phys Lett 92:152907
4. Shannigrahi SR, Huang A, Chandrasekhar N, Tripathy D, Adeyeye AO (2007) Appl Phys Lett 90:022901
5. Takahashi K, Kida N, Tonouchi M (2006) Phys Rev Lett 96:117402
6. Gao F, Chen XY, Yin KB, Dong S, Ren ZF, Yuan F, Yu T, Zou ZG (2007) Adv Mater 19:2889
7. Simões AZ, Cavalcante LS, Riccardi CS, Varela JA, Longo E (2008) Curr Appl Phys. doi:10.1016/j.cap.2008.05.001
8. Ederer C, Spaldin NA (2005) Phys Rev B 71:060401
9. Wang Y, Nan CW (2008) J Appl Phys 103:024103
10. Hu GD, Cheng X, Wu WB, Yang CH (2007) Appl Phys Lett 91:232909
11. Wang Y, Nan CW (2006) Appl Phys Lett 89:052903
12. Singh SK, Sato K, Maruyama K, Ishiwara H (2006) Jpn J Appl Phys Part 2 45:L1087
13. Lee CC, Wu JM (2007) Electrochem Solid State 10:G58
14. Kartopu G, Lahmar A, Habouti S, Solterbeck CL, Elouadi B, Souni ME (2008) Appl Phys Lett 92:151910
15. Cheng ZX, Wang XL, Dou SX, Kimura H, Ozawa K (2008) Phys Rev B 77:092101
16. Zhang BS, Quan ZC, Zhang TJ, Guo T, Mo SB (2007) J Appl Phys 101:014107
17. Moulder JF, Stickle WF, Sobol PE, Bomben KD (1992) Handbook of X-ray photoelectron spectroscopy. Perkin-Elmer Corporation, Minnesota
18. Wang YP, Zhou L, Zhang MF, Chen XY, Liu JM, Liu ZG (2004) Appl Phys Lett 84:1731
19. Brinkman K, Iijima T, Nishida K, Katoda T, Funakubo H (2007) Ferroelectrics 357:599
20. Brinkman K, Iijima T, Takamura H (2007) Jpn J Appl Phys Part 2 46:93
21. Schaffer JP, Saxena A, Antolovich SD, Sanders TH, Warner JSB (1999) The science and design of engineering materials, 2nd edn. McGraw-Hill Companies, New York
22. Wang J, Neaton JB, Zheng H, Nagarajan V, Ogale SB, Liu B, Viehland D, Vaithyanathan V, Schlom DG, Waghmare UV, Spaldin NA, Rabe KM, Wuttig M, Ramesh R (2003) Science 299:1719
23. Gao YH, Shen H, Ma JH, Xue JQ, Sun JL, Meng XJ, Chu JH, Wang PN (2007) J Appl Phys 102:064106
24. Askeland DR (1994) The science and engineering of materials, 3rd edn. PWS Publishing Company, Boston
25. Wang Y, Jiang QH, He HC, Nan CW (2006) Appl Phys Lett 88:142503
26. Talik E, Guzik A (2003) Phys Stat Sol (a) 196:332
27. Qi XD, Dho J, Tomov R, Blamire MG, MacManus-Driscoll JL (2005) Appl Phys Lett 86:062903